Rigid Motion Tracking using Moments of Inertia in TOF-PET Brain Studies

Ahmadreza Rezaei[1], Matthew Spangler-Bickell[2], Georg Schramm[1], Koen Van Laere[1], Johan Nuyts[1], and Michel Defrise[3]

[1]KU Leuven - University of Leuven, Department of Imaging and Pathology, Nuclear Medicine & Molecular imaging; Medical Imaging Research Center (MIRC), B-3000, Leuven, Belgium. [2]PET/MR Engineering, GE Healthcare, Waukesha, WI, USA. [3]Department of Nuclear Medicine, Vrije Universiteit Brussel, B-1090, Brussels, Belgium.

E-mail: ahmadreza.rezaei@uz.kuleuven.be

Abstract. A data-driven method is proposed for rigid motion estimation directly from TOF-PET emission data. Rigid motion parameters (translations and rotations) are estimated from the first and second moments of the emission data masked in a spherical volume. The accuracy of the method is analyzed on 3D analytical simulations of the PET-SORTEO brain phantom, and subsequently tested on ^{18}F-FDG as well as ^{11}C-PIB brain datasets acquired on a TOF-PET/CT scanner. The estimated inertia-based motion is later compared to rigid motion parameters obtained by directly registering the short frame backprojections. We find that the method provides sub mm/degree accuracies for the estimated rigid motion parameters for counts corresponding to typical 0.5 s, 1 s, and 2 s ^{18}F-FDG brain scans, with the current TOF resolutions clinically available. The method provides robust motion estimation for different types of patient motion, most notably for a continuous patient motion case where conventional frame-based approaches which rely on little to no intra-frame motion of short time intervals could fail. The method relies on the detection of stable eigenvectors for accurate motion estimation, and a monitoring of this condition can reveal time-frames where the motion estimation is less accurate, such as in dynamic PET studies.

Keywords: Time-of-Flight Positron Emission Tomography, Brain Imaging, Data-driven Motion Estimation, Rigid Motion Correction

1. Introduction

Patient motion affects image quality and diagnostic accuracy of PET brain imaging, in particular in subjects for whom it is difficult to lie still for several minutes, such as children, elderly subjects and subjects with neurological disorders (e.g. Alzheimer's or Parkinson's disease). In state-of-the-art brain positron emission tomography (PET), where acquisitions can last up to 120 min (Firouzian et al. 2018; Kolinger et al. 2021), subject motion is an important source of image artefacts. Even with the use

of positioning aids and head restraints, displacements of 2 mm - 5 mm and rotations of 2° - 3° are common and larger magnitudes are expected without restraint or if non-customized supports are used (Kyme et al. 2021). Patient motion can result in a loss of resolution or misplacement of structures in the reconstructed tomographic image (Herzog et al. 2005) and introduce bias on the estimated tracer kinetic parameters in dynamic brain studies (Jin et al. 2013b). The impact of motion on local metabolic quantification (Ruttimann et al. 1995) despite the use of head restraints has been shown as early as 1995. In view of the limited spatial resolution (7.5 mm FWHM in-plane, 10.5 mm FWHM axial) of the scanner, a stronger impact is to be expected with a spatial resolution around 2.5 mm for dedicated brain scanners (de Jong et al. 2007) and around 3.5 mm for state-of-the-art clinical scanners (van Sluis et al. 2019). Consequently, motion on the order of only a few mm can adversely affect the spatial resolution, and its correction becomes increasingly important. There is currently no established motion compensation method for clinical PET brain imaging, and the system software of modern state-of-the-art PET systems does not provide motion compensation for this application.

Rigid motion compensation for brain PET acquisitions has already been performed by several groups (Menke et al. 1996; Goldstein et al. 1997; Lopresti et al. 1999; Fulton et al. 2000; Fulton et al. 2003; Buhler et al. 2004; Carson et al. 2003; Rahmim et al. 2004; Jin et al. 2013a; Olesen et al. 2013; Spangler-Bickell et al. 2019). In most cases, the motion of markers that were attached to the head of the subject were tracked with optical (or infrared) cameras with a high temporal resolution (ca. 30 Hz). The derived rigid motion information is then used to correct the recorded information of each detected photon pair in a listmode PET reconstruction. Besides limiting patient comfort during the PET acquisition, the use of markers bears the risk of inaccurate motion tracking as the markers are either attached to the skin or to a cap which the patient wears during the scan. Consequently, motion of the marker relative to the head can occur, which can cause deviations between the tracked and the true head motion. Moreover, the accurate positioning of the markers prolongs and complicates the PET exam, which is likely the reason why there is still no commercial solution for use in clinical routine, despite the promising results of rigid motion compensation for PET acquisitions of the brain. With major advances in the field of human face tracking and face recognition, novel marker-less motion tracking techniques were introduced (Noonan et al. 2015; Kyme et al. 2018). However their use has also been limited as they require changes to the scanning protocol, need careful positioning of the cameras within the scanner bore, and more importantly, most of the available motion tracking hardware are not suitable for use in the strong magnetic field of the PET/MR.

In this work we focus on data-driven methods, which do not require any additional hardware. There is an abundance of data-driven rigid and non-rigid motion correction techniques in PET (Ren et al. 2017; Lu et al. 2020; Spangler-Bickell et al. 2021; Panin 2021), with the majority of these methods relying on a motion trace which is used to divide the emission data in motion-free or static frames where preliminary reconstructions are generated and subsequently registered for the motion estimation.

Focusing on rigid motion correction for the brain, recently, the center of distribution of events (computed in short 1 s time-frames) has been shown to be a reliable trace for the classification of the data into static frames (Lu et al. 2020). Similar to (Spangler-Bickell et al. 2021), our proposed method divides the emission data in a series of short "static" frames, but then directly estimates estimates rigid motion parameters from the emission data, avoiding the typically necessary reconstructions/registrations of other methods. Improving on the works of (Feng et al. 2016), we exploit the localization provided by the TOF measurements to compute the full 6 degrees of freedom of a rigid transform from the first and second moments of inertia of the TOF events, avoiding the additional data rebinning, histograming and projection-based processing for the inertia estimation. The inter-frame translations and rotations are then estimated as differences of the first moments and the solution to the Procrustes problem of the second moments, respectively. Although due to practical reasons rigid motion parameters were computed from moments of inertia which in turn were computed from backprojections of the short "static" frames, we will demonstrate that the moments of inertia can be computed directly from the most-likely annihilation position of the measured events, which will allow rapid motion estimation. By incorporating a soft masking scheme for the estimation of the first and second moments, problems due to axial truncation of the data as well as problems caused by non-moving body parts like the neck and shoulders are mitigated. Results on 3D simulations and patient data show that reliable motion estimates comparable to registration-based motion estimates can be computed directly from the TOF emission data for most common tracers. Furthermore, this approach provides accurate motion estimates in patient scans with continuous motion where defining static frames can be challenging, and can provide a measure for the accuracy of the motion estimates. The paper is organized as follows: in section 2 the motion estimation approach is discussed. Section 3 describes the 3D simulation and patient studies which we use to validate the method. The results of our studies are then shown in section 4 and discussed in section 5.

2. Methods

With continuous improvements in the time resolution of time-of-flight (TOF) PET scanners, more localized information of tracer densities becomes available from the emission measurements, which the moment of inertia can be computed from. These moments of inertia can then be analyzed to track rigid patient motion during the scan.

2.1. First Moment; Translation

The first moment of inertia of an object defines its center of mass (COM):

$$\vec{I} = [I_x\, I_y\, I_z] \tag{1}$$

where I_i, $i = x, y, z$ are the COM vector elements in Cartesian spatial coordinates, and are computed from the most-likely annihilation point $\vec{x}_e = (x_e, y_e, z_e)$ of all the events e

(normalized for its axial sensitivity d_e) within a defined time-frame as:

$$I_i^{(t)} = \frac{1}{\sum_{e\in t} w_e\, d_e} \sum_{e\in t} w_e\, d_e\, i_e, \quad i = x, y, z \tag{2}$$

where t denotes the time-frame and w_e is a weight defined below in Algorithm 1.

To suppress the influence of "background" events, the weights w_e are introduced in (2) to restrict the COM contributions to events detected within a (fuzzy) spherical volume. Algorithm 1 defines our implementation for computing the COM from a volume with a decreasing radius $r \in [R_0, R_1]$ with step sizes of R_s (parameters defined in section 2.3). Once a reference frame is chosen, the 3 translational degrees of freedom are given by the difference between the COMs of the current and reference frames.

Algorithm 1: Computing the COM

```
define R_0, R_1, R_s and b;
initialize I^(t) using (2) with w_e = 1 ∀e ∈ t and set r = R_0;
while r > R_1 do
    for i = 1, ..., 3 do
        w_e = erfc( (||x^(t) − I^(t)|| − r)/b ) /2
        /* where erfc is the complementary error function and b
           determines the transition width from 1 to 0.          */
        update I^(t) using (2) with w_e
    end
    r ← r − R_s
end
```

2.2. Second Moments; Rotation

The second moment of inertia of a body around a particular rotation axis is calculated by an infinite sum weighted by its infinitesimal densities. Define the inertia tensor $\mathbf{I}$ as,

$$\mathbf{I} = \begin{bmatrix} I_{xx} & I_{xy} & I_{xz} \\ I_{yx} & I_{yy} & I_{yz} \\ I_{xz} & I_{yz} & I_{zz} \end{bmatrix} \tag{3}$$

where the I_{ij}, $i, j = x, y, z$ components are computed from the most-likely position $\vec{x}_e$ corrected for the COM, i.e. $\vec{x}_e - \vec{I} = (x'_e, y'_e, z'_e)$ as:

$$I_{xx} = \frac{1}{\sum_{e\in t} w_e\, d_e} \sum_{e\in t} w_e\, d_e\, (y_e'^2 + z_e'^2), \quad I_{xy} = I_{yx} = \frac{-1}{\sum_{e\in t} w_e\, d_e} \sum_{e\in t} w_e\, d_e\, x'_e\, y'_e,$$

$$I_{yy} = \frac{1}{\sum_{e\in t} w_e\, d_e} \sum_{e\in t} w_e\, d_e\, (x_e'^2 + z_e'^2), \quad I_{xz} = I_{zx} = \frac{-1}{\sum_{e\in t} w_e\, d_e} \sum_{e\in t} w_e\, d_e\, x'_e\, z'_e,$$

$$I_{zz} = \frac{1}{\sum_{e\in t} w_e\, d_e} \sum_{e\in t} w_e\, d_e\, (x_e'^2 + y_e'^2), \quad I_{yz} = I_{zy} = \frac{-1}{\sum_{e\in t} w_e\, d_e} \sum_{e\in t} w_e\, d_e\, y'_e\, z'_e.$$

Computing the inertia tensors from the most-likely annihilation positions $\vec{x}_e$ (or alternatively from backprojections) introduces a geometry and TOF resolution dependent bias term. Section 7 provides more details on the estimation of the first (10) and second (13), (14), (15) moments of inertia from the measured emission data. As before, the inertia tensors were computed in the sphere of the smaller radius (R_1) defined in the COM calculation.

The relationship between the inertia tensor of an object at an instant t to a reference time point t_0 is:

$$\mathbf{I}^{(t)} = \mathbf{R}^T \mathbf{I}^{(t_0)} \mathbf{R} \tag{4}$$

where ^{T} denotes a matrix transpose, and $\mathbf{R}$ is the 3×3 rotation matrix. The problem of solving (4) to estimate $\mathbf{R}$ from $\mathbf{I}^{(t)}$ and $\mathbf{I}^{(t_0)}$ is the classical orthogonal Procrustes problem (Schönemann 1966), which can be solved by an eigenvalue decomposition of the two tensors.

2.3. Implementation

The last frame of the acquisition was chosen as the frame of reference, which all the inertia moments were compared to. The COMs were computed using $R_0 = 11.5$ cm to a radius of $R_1 = 9.0$ cm with steps of $R_s = 0.5$ cm, and the transition width b was heuristically set to 1.0 cm which provided satisfactory results. This masking of the emission measurements proved to be an effective approach for avoiding potential pitfalls due to data truncation. The inertia tensors were computed from TOF-backprojections as opposed to the most-likely annihilation positions, because the time-of-flight information in the listmode emission data only provided TOF information with the standard sinogram TOF-sampling of 169.26 ps as opposed to the initial fine TOF-sampling of 13.02 ps used by the acquisition electronics. In earlier motion estimation attempts, this coarser sampling of the TOF information created undesirable effects as the most-likely annihilations positions of the coarsely sampled TOF data no longer uniformly sample the imaging volume but are structured as rings along the axial dimension of the scanner. Following TOF backprojections, the volume was corrected for the axial sensitivity of the scanner (Hsu et al. 2017) using a pre-computed non-TOF backprojection of a sinogram of all ones (using the voxel intensities as a_e). Although the effect of the bias on the estimated inertia tensors could be approximated and used during the estimation of the rotation parameters, this correction was not applied as accurate results were obtained when this term was ignored. The rotation parameters were computed by diagonalizing the inertia tensors, sorting the eigenvalues and flipping the direction of the eigenvectors, if necessary.

2.4. Motion Tracking Accuracy

In this work, the 6 degrees of freedom of the rigid transform are estimated assuming that the eigenvectors of the tracer distribution remain fixed during brain scans in all

different time-frames. However, this assumption most-likely would not hold in dynamic scans with fast kinetics as well as in cases where the patient moves partly outside of the scanner field of view. Furthermore, the rigid motion estimation relies twice on the accuracy of the estimated COM for each frame, directly through translations and indirectly through the estimation of the inertia tensor (and hence rotations). For the latter, inaccuracies in the estimated COM can cause deviations to the direction of the estimated eigenvectors. With typical tracer distributions of common tracers, these effects may manifest in the length of the estimated eigenvectors, i.e. inertia tensor eigenvalues. Hence we propose to use the eigenvalues computed through the scan to monitor the accuracy of the estimated rigid motion parameters, by first checking whether or not the diagonalization of the inertia tensor provides distinct eigenvalues, and second by monitoring their evolution to detect unreliable motion frames.

2.5. Image Reconstruction

A listmode ordered subsets expectation maximization (OSEM) reconstruction with a motion-aware system matrix was applied to reconstruct a single activity image. An initial reconstruction of the activity ignoring attenuation was generated and used to align the CT-based attenuation image to the activity frame of reference. To accelerate the motion reconstruction procedure (and to avoid full backprojections of the attenuation at each time-frame), the activity reconstructions were obtained pre-correcting for the attenuation ($a_{l'}$) along motion-corrected lines-of-response (LORs) $l' = \mathcal{G}_t^{-1}(l)$ where the end-points of LOR l have been transformed by the rigid parameters computed at time-frame t. The attenuation correction factors were obtained by projecting the aligned CT-based attenuation image along motion-corrected LORs, and a motion-averaged sensitivity image was created by averaging a static sensitivity image over the motion computed in each time-frame (Rahmim et al. 2004). The activity reconstruction was updated using,

$$\lambda_k^{(n+1)} = \frac{\lambda_k^{(n)}}{\sum_t \mathcal{G}_t \left(\sum_{l\tau} c_{lk\tau} O_{l\tau}\right)} \sum_{l\tau} c_{l'k\tau} \frac{1.0/a_{l'}}{\sum_\psi c_{l'\psi\tau}\lambda_\psi^{(n)} + s_{l\tau}/a_{l'}} \tag{5}$$

where λ_k is the activity reconstruction at voxel k and n represents the iterations. The sensitivity of TOF-bin τ along LOR l to emissions from voxel k (including detector-pair sensitivities) is denoted by $c_{lk\tau}$, O is a TOF-sinogram of all ones, $s_{l\tau}$ is the additive contribution of randoms and scatter for data-bin $(l\tau)$. Note that the additive contribution is indexed with l (as opposed to l') as randoms and scatter are computed over the entire scan duration and not at each time-frame. Ordered subsets were implemented using every q-th (number of subsets) event.

3. Experiment Design

In addition to analyzing the motion estimation technique on the PET-SORTEO brain phantom (Reilhac et al. 2005), the proposed method is applied to patient brain scans

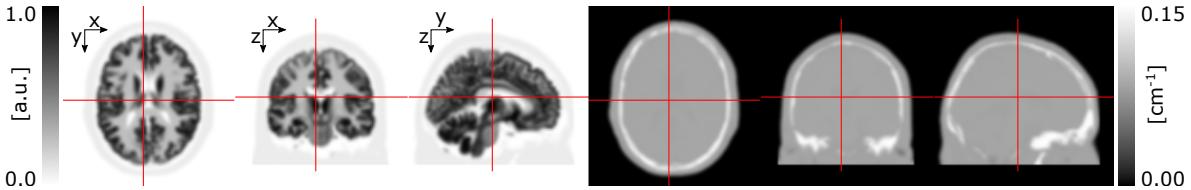

Figure 1: PET-SORTEO activity and attenuation images used for the 3D simulation.

acquired on the GE Discovery MI TOF-PET/CT scanner at our institution. Results obtained from the patient datasets are compared to the rigid motion computed by directly registering the short frame backprojections. The data analysis software and the subsequent listmode OSEM reconstruction of the patient data have been obtained using in-house registration and reconstruction tools.

3.1. 3D Brain Simulation

Using the GE Discovery MI specifications (Hsu et al. 2017), emission data were generated from the PET-SORTEO phantom shown in figure 1. The simulated TOF-PET data were generated using the activity and attenuation images shown and subsequently scaled to have 500K counts, corresponding to a 1 s acquisition of a typical patient ^{18}F-FDG brain scan. The total counts include a uniform additive contribution to yield a 25% ratio of randoms to true events. A set of 16 datasets‡ were generated, and Poisson noise was subsequently added to the TOF measurements. In all but the reference frame (15 datasets), the scanner LOR end-points were rigidly transformed (up to a maximum of $\pm$22.5 degrees and $\pm$50 mm rotations and translations, respectively) to simulate patient motion, and no truncation (activity moving outside the field of view (FOV)) was simulated in this study. The data were subsequently backprojected, correcting for the axial sensitivity of the scanner, and used to compute the first and second moments of inertia. The computed moments of inertia were later compared to the ones obtained at the original scanner positioning, and the estimated rigid motion parameters were compared to the applied rigid transform. For the estimation of each rigid motion transform 12 noise realizations were simulated. Furthermore, the simulations were repeated with 250K and 1M count datasets to analyze the accuracy of the motion estimates at varying count rates.

3.2. Patient Data

For this study, we used PET-scans from two patients injected with 291.0 MBq and 231.6 MBq of ^{18}F-FDG and from a patient injected with 317.0 MBq of ^{11}C-PIB, who where scanned on the GE Discovery MI TOF-PET/CT. The two ^{18}F-FDG and ^{11}C-PIB patient brain scans were acquired 90 and 30 minutes post-injection for a duration of 15

‡ In this study, the data format (sinogram or listmode) in which the moments of inertia are computed from is irrelevant. Using the sinogram data format allows easier inclusion of Poisson noise to the data.

and 20 minutes, and had an average count rate of 489.6K counts/s, 384.3K counts/s and 54.7K counts/s, respectively. The GE PET Reconstruction Toolbox was used to estimate the scatter contribution using CT-based attenuation images. Scatter and randoms contributions were estimated from the measured data over the entire scan duration. Backprojections were computed in a voxel grid of 70×70×40 of 5×5×5 mm^3 widths. The estimated inertia-based motion parameters were then compared to motion parameters computed by rigid registration of the backprojections using either the sum of squared differences (SSD) or normalized mutual information (NMI) as the alignment cost function (Hill et al. 2001). The intramodal nature of the registrations at different time-frames motivated the use of SSD for image alignment, and accounting for tracer dynamics inspired comparisons to motion estimation using NMI. The backprojections used for registration were not masked and the motion parameters were estimated from the measured activity within the entire FOV of the scanner.

Once the rigid parameters were estimated, the emission end-points of listmode events within a given time-frame were transformed using its corresponding motion estimate. For each scan, a single activity image was reconstructed from the motion corrected listmode events of the entire scan data with the listmode OSEM algorithm using 4 iterations of 34 subsets. The tracer activity images were reconstructed in a finer voxel grid of 192×192×71 of 1.6×1.6×2.79 mm^3. The 3 motion corrected OSEM reconstructions (inertia, NMI, and SSD) are shown after alignment to the non motion-corrected reconstruction.

4. Results

4.1. Simulations

Figure 2 shows absolute errors of the estimated rigid parameters when compared to the ground truth, computed over all noise realizations and the set of 15 different rigid parameter sets (non simulating data truncation). T_X, T_Y and T_Z are translations in the spatial coordinates x, y and z, defined in figure 1, and rotations along the three axes are denoted by R_{YZ}, R_{XZ} and R_{XY}, respectively. We observe that the moments of inertia provide an accurate estimate of the rigid transformations present between the 3D simulated frames even when the scanner dependent bias term of the inertia tensor is ignored. With increasing counts, the accuracy of the motion estimation increases.

4.2. Patient Data

Figures 3 and 4 show the results obtained for the two ^{18}F-FDG patient datasets. As would be expected, both motion corrected datasets are diagnostically superior to the non-corrected reconstructions, as judged by clinicians in our institute. The rigid motion parameters estimated for these two patient datasets show two different types of possible patient motion during PET scans. Whereas in figure 3 we observe erratic motion with motion-free intervals, the motion parameters of figure 4 show a more continuous motion

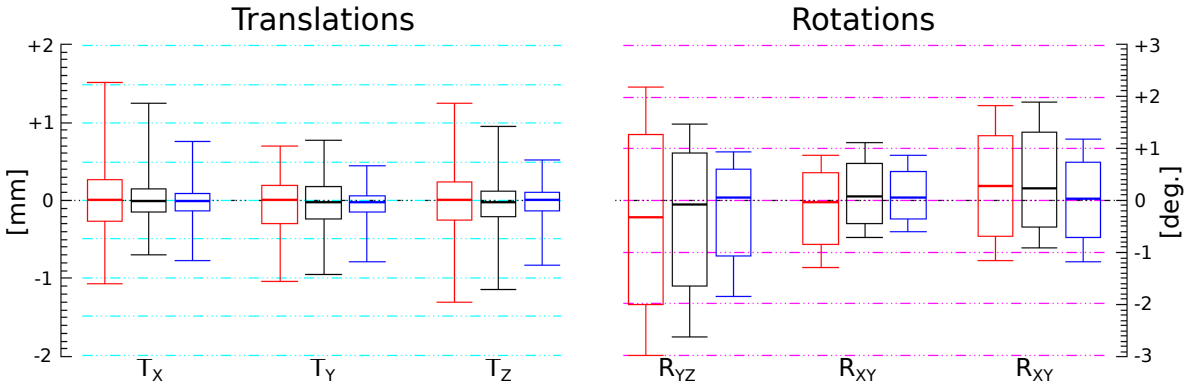

Figure 2: Absolute errors of the estimated rigid parameters of the 250K (red), 500K (black) and 1M (blue) count simulations computed over 12 noise realizations for 15 parameter sets when compared to the ground truth. The boxplots show the minimum, lower quartile, median, upper quartile and maximum of the absolute errors.

pattern during data acquisition. Although dividing the entire scan in subsets of motion-free intervals for frame-wise reconstruction is relatively straight forward for the patient dataset of figure 3, splitting the TOF-PET emission data for the patient dataset shown in figure 4 is more challenging.

The eigenvalues computed from the inertia tensors of the ^{18}F-FDG scans seem relatively stable with limited drift. Some sharp changes can however be seen in the estimated eigenvalues of figure 3, which correspond to sudden strong patient motions. For both datasets, the inertia-based motion corrected reconstructions are visually comparable to the registration-based (NMI and SSD) motion corrected reconstructions.

Figure 5 shows the results obtained on the ^{11}C-PIB patient brain dataset. Although the emission data are noisier than the ^{18}F-FDG datasets, the estimated eigenvalues are distinct and relatively stable during the scan except for the frames with erratic patient motion. Apart from the amount of noise on the three motion parameter sets computed from the 5 s, 1 s and 0.5 s time-frames, the parameter sets agree on the extent of the patient motion. Contrary to the ^{18}F-FDG results, the registration-based methods slightly disagree on the amount of motion for the second half of the patient scan. Unfortunately there is no ground truth to compare the reconstructions to, however visually the inertia-based reconstruction seems slightly sharper particularly at the midline of the brain. Further evidence of this is that the eigenvalues computed for the first and second half of the scan are in agreement in the time intervals unaffected by motion.

The amount of motion on a subset (acquired on the TOF-PET/CT) of patient brain scans processed, which was either suspect to patient motion (as judged by the technical staff) or selected for motion correction by the physician, is shown in figure 6. The relative motion was computed from 5s inertia-based motion parameters, minimizing effects of noise, and compared to the frame which the COG was most stationary. In this collection of brain scans 18 cases have tranlations/rotations exceeding 5 mm/degree.

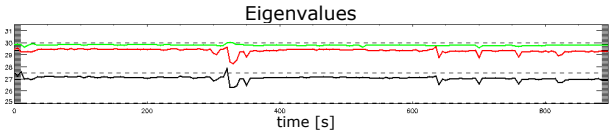

(a) Eigenvalues computed from the 5 s frame inertia tensors.

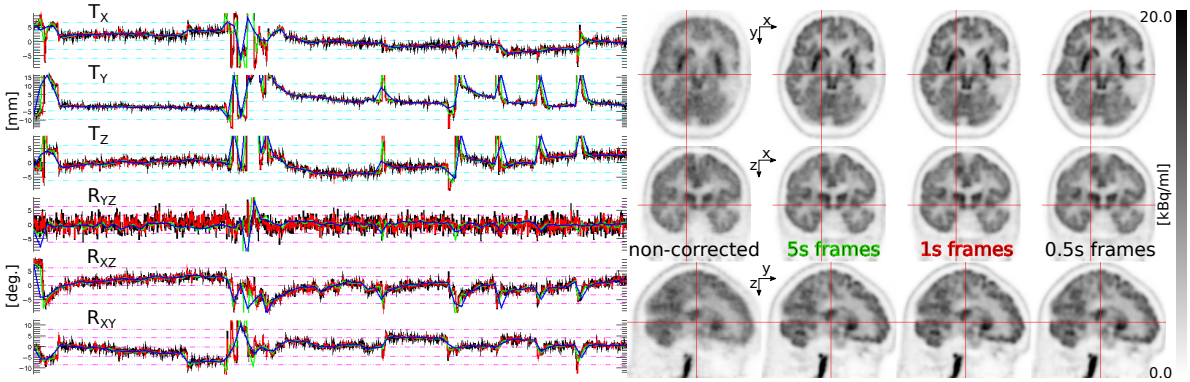

(b) Left: motion traces computed from 5 s (green), 1 s (red), and 0.5 s (black) frame inertia moments. Right: transaxial (top), coronal (center) and sagittal (bottom) views of OSEM activity reconstruction corrected for motion using the estimated rigid transforms (left).

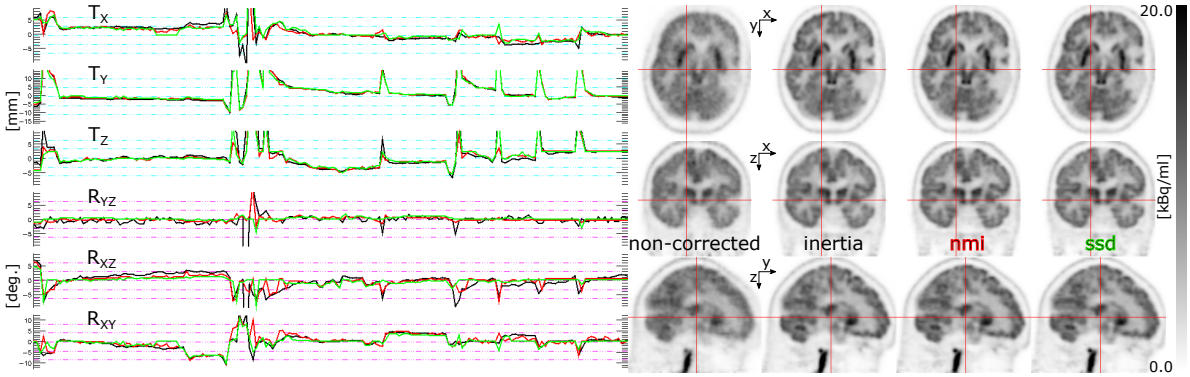

(c) Left: motion traces computed from 5 s frames using the inertia moments (black), normalized mutual information (red) and sum of squared differences (green). Right: transaxial (top), coronal (center) and sagittal (bottom) views of OSEM activity reconstruction corrected for motion using the estimated rigid transforms (left).

Figure 3: ^{18}F-FDG patient brain scan dataset.

Note that cases 16, 19 and 22 correspond to motion profiles shown in figures 5, 4 and 3, respectively. Furthermore, for visual assessment of patient motion, GIF files (applying the estimated 1 s motion parameters to the inertia-based motion corrected reconstruction) for the 3 patient datasets are available as supplementary material.

5. Discussion

There has been a collection of recent works on the use of the first moment of inertia of the PET emission data in short frame durations for the detection of frames with limited

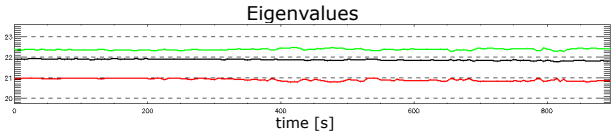

(a) Eigenvalues computed from the 5 s frame inertia tensors.

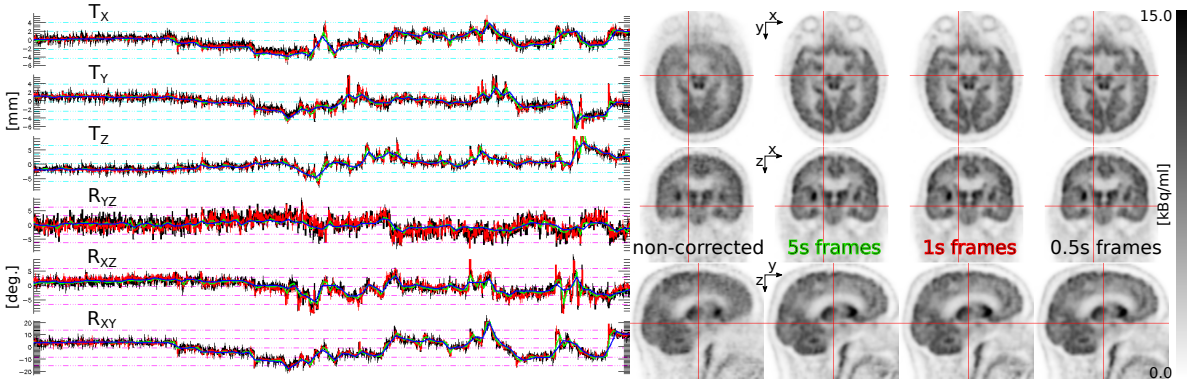

(b) Left: motion traces computed from 5 s (green), 1 s (red), and 0.5 s (black) frame inertia moments. Right: transaxial (top), coronal (center) and sagittal (bottom) views of OSEM activity reconstruction corrected for motion using the estimated rigid transforms (left).

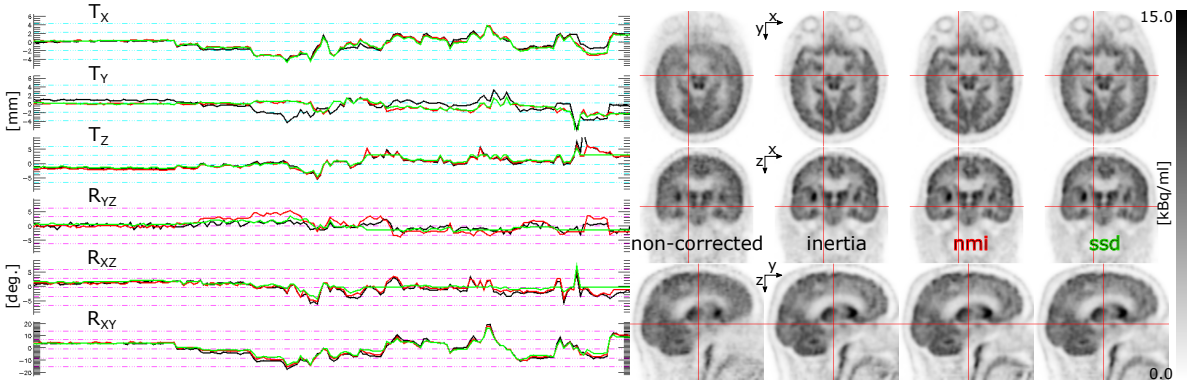

(c) Left: motion traces computed from 5 s frames using the inertia moments (black), normalized mutual information (red) and sum of squared differences (green). Right: transaxial (top), coronal (center) and sagittal (bottom) views of OSEM activity reconstruction corrected for motion using the estimated rigid transforms (left).

Figure 4: ^{18}F-FDG patient brain scan dataset.

intra-frame motion (Lu et al. 2020; Ren et al. 2017). In most of the studies, the motion parameters are subsequently estimated by registering reconstructions of the motion-free frames to the reconstruction of a reference frame. In this work, similar to the work by (Feng et al. 2016), we directly estimate rigid motion parameters by analyzing the spread of the tracer distribution in the PET emission data. We estimate the moments of inertia directly and rapidly from the localized TOF information, eliminating the need for histogrammed projections. The method does not require reconstructions and the subsequent registration for motion estimation, hence, it is computationally very efficient. In our implementation (and for a dataset for which the fine TOF-sampling

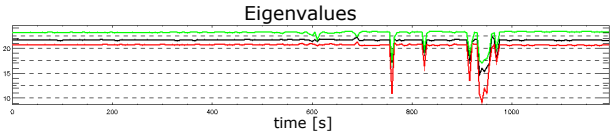

(a) Eigenvalues computed from the 5 s frame inertia tensors.

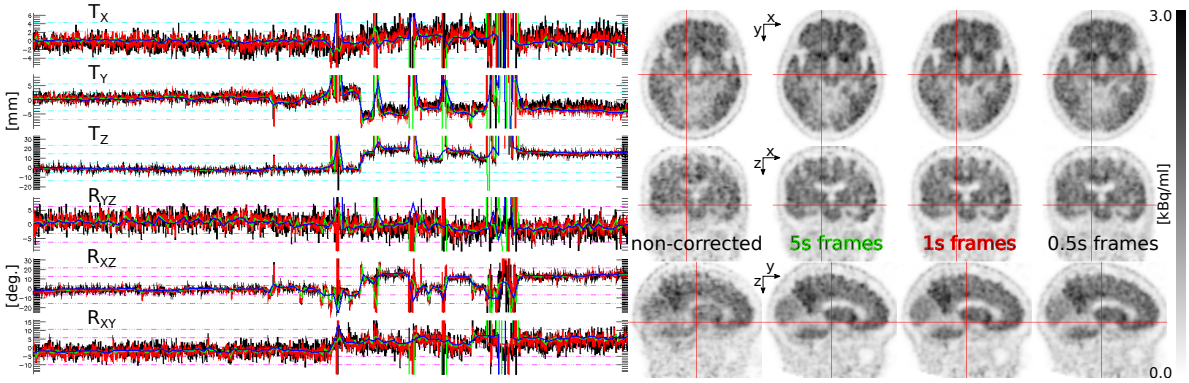

(b) Left: motion traces computed from 5 s (green), 1 s (red), and 0.5 s (black) frame inertia moments. Right: OSEM activity reconstruction corrected for motion using the estimated rigid transforms.

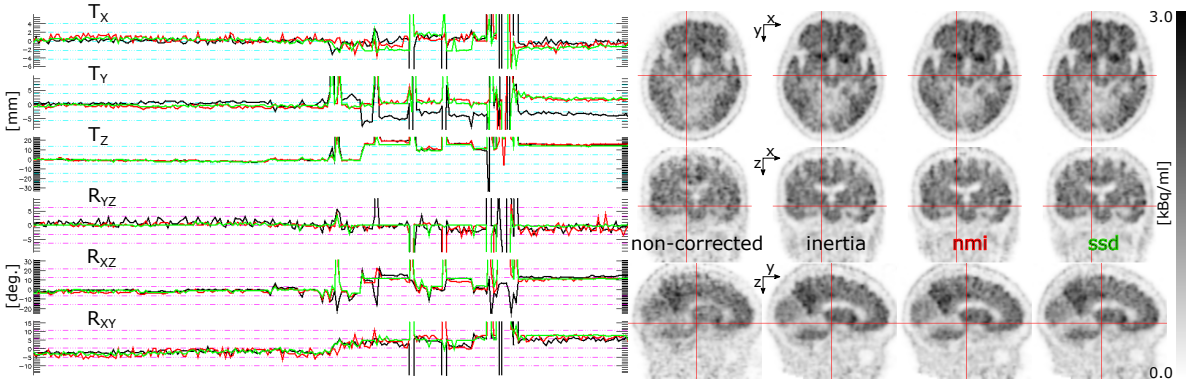

(c) Left: motion traces computed from 5 s frames using the inertia moments (black), normalized mutual information (red) and sum of squared differences (green). Right: transaxial (top), coronal (center) and sagittal (bottom) views of OSEM activity reconstruction corrected for motion using the estimated rigid transforms (left).

Figure 5: ^{11}C-PIB patient brain scan dataset.

measurements were available), motion estimation from backprojections as opposed to the most-likely position of events increased the computation time by 122.6%, and was further increased by 17.8% and 25.1% for the 3D volume registrations using SSD and NMI, respectively. In an initial stage the center of mass of the tracer distribution is computed and refined within a sphere with a pre-determined radius. The second moment of inertia is then calculated from the emission data and subsequently rigid motion parameters are computed by diagonalizing the inertia tensors.

In this study, we have assumed the background contributions to be negligible and ignored the effect of scatter and randoms events during motion estimation. Breaking the inertia tensor of the measurements into the sum of trues, scatter and randoms inertia

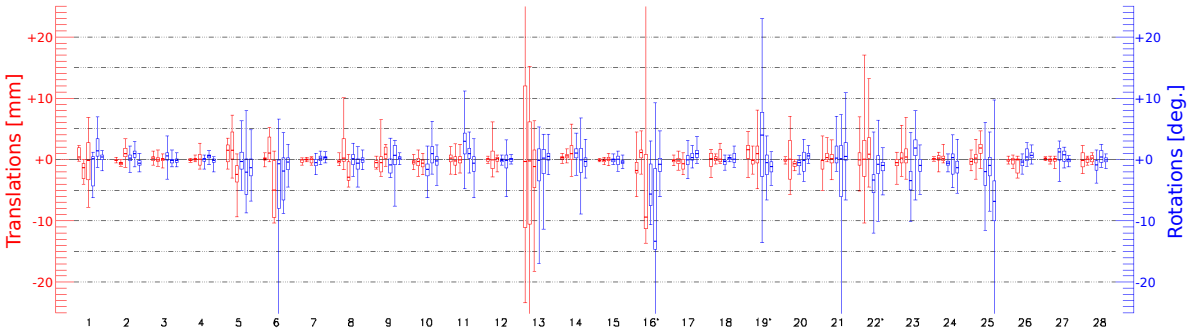

Figure 6: Boxplots showing the minimum, lower quartile, median, upper quartile and maximum of the relative inter-frame motion (differences in T_X,T_Y,T_Z,R_{YZ},R_{XZ} and R_{XY} from left to right, respectively) as compared to a reference frame.

tensors, in the noise-less case, we expect the randoms tensor to have identical eigenvalues and the scatter tensor to be affected similarly as the trues tensor. However, scatter and randoms tensors computed in short time-frames, will contribute to the noise of the emission tensor and hence the estimated motion. We found the spherical masking of the emission events, which works in a similar manner to a fuzzy k-means clustering of a single cluster, to be effective in mitigating problems related to background emissions and to the axial truncation of the emission data. Furthermore, as computing the scatter estimate in each time-frame (for motion corrected LORs l') is impractical, we are correcting for scatter using the simulated scatter estimate of the entire static scan. We do not expect inaccuracies due to this with "moderate" patient motion as the scatter is expected to be fairly smooth. However, with "larger" patient motion it would possibly be best to consider a dynamic estimate of the background contribution.

We find that although the inertia tensor of the TOF-PET emission data provides a biased estimate of the tracer distribution tensor, accurate rigid motion parameters can still be obtained ignoring the scanner-dependent bias term. Since the bias tensor is quadratically proportional to the TOF resolution of the scanner, it will have a decreasing effect with improvements in the TOF resolution of future scanners. Our 3D simulation study shows that the rigid motion parameters can be computed with increasing accuracy with higher counts within the short time-frames.

A collection of more than 30 (and growing) number of patient brain scans acquired on the TOF-PET/CT and TOF-PET/MR have been analyzed using the proposed method. These studies demonstrate that the data-driven motion estimation can be utilized on a variety of tracers. However, the approach can be sub-optimal when the tracer's spatial distribution has an isotropic inertia tensor, or in cases where the brain is moved out of the scanner's FOV. Fortunately, the method provides a means (the eigenvalues) to quantify the accuracy of the motion estimations. In the current study, the entire scan data and the rigid motion parameters have been used for the tracer activity reconstruction. Further analysis of the measured eigenvalues of the inertia tensors can be used to detect cases where the approach is sub-optimal or to discard

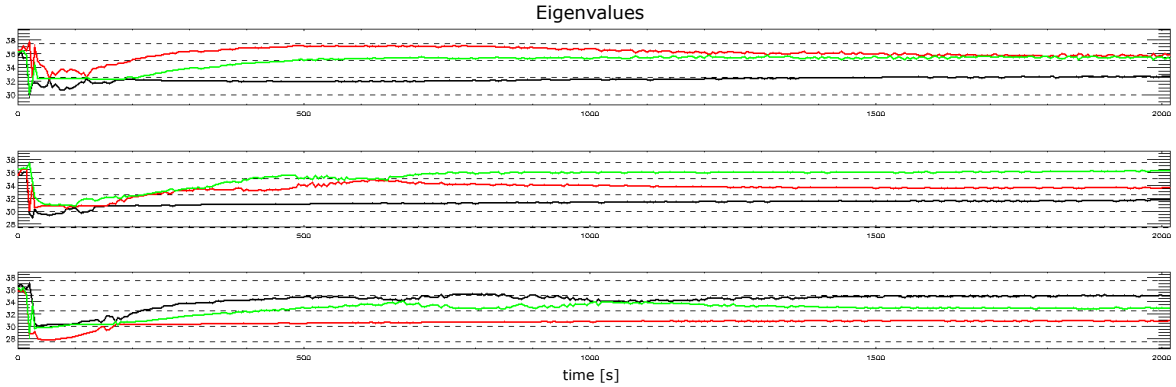

Figure 7: Eigenvalues computed from 15 s frame inertia tensors of 3 dynamic ^{18}F-FDG patient datasets.

data for which the motion estimates are inaccurate.

As with many data-driven motion correction methods, the proposed method might not be well suited for the analysis of motion in dynamic studies. In such studies, analysis of the estimated eigenvalues can provide an accuracy measure for the estimated rigid motion. As an example, figure 7 shows the eigenvalues computed for three dynamic scans where low levels of patient motion were expected. It is expected that the rigid motion parameters are reliably estimated in the intervals where the eigenvalues have plateaued, and less so for the initial frames. Analysis of the motion estimation accuracy in dynamically changing frames will be the topic of future studies.

6. Conclusion

In this work we propose a data-driven rigid motion tracking approach for TOF-PET brain studies. The motion tracking approach extends previous work by Feng et al. 2016, which uses moments of inertia for motion estimation. Our method relies on the TOF resolution of PET scanners, and we find that the rigid motion parameters can be reliably estimated from TOF-PET emission data obtained on a 400 ps FWHM TOF resolution system. We demonstrate how the method is currently being used for motion correction at our center on various tracer acquisitions. We find that patient motion can be estimated with a temporal sampling of 1 s or even better, which could possibly even be used for motion detection and correction of MR in hybrid PET/MR scanners. Although the proposed motion tracking strategy is not well suited for dynamic studies with fast kinetics, as with most data-driven motion estimation techniques, it provides a measure where accurate motion estimation should be expected.

Acknowledgements

The authors would like to thank Floris Jansen and Timothy Deller from GE Healthcare for their help and support, and also Kris Thielemans who brought to our attention

the work by Feng et al. 2016. This work was supported in part by the Research Foundation Flanders (FWO) project G062220N and by the Center for Advanced Imaging Innovation and Research, a National Institute for Biomedical Imaging and Bioengineering Biomedical Technology Resource Center (NIH P41 EB017183).

7. Appendix

7.1. Listmode Data

Assume $w(t)$ is a gaussian TOF profile with known standard deviation $\sigma < \infty$,

$$w(t) = e^{-t^2/(2\sigma^2)}/\sqrt{2\pi}\sigma. \tag{6}$$

In listmode data acquisition, one detects N events $e = 1, \ldots, N$ parameterized by their orientation unit vector $\vec{\alpha}_e$ and most-likely annihilation point $\vec{x}_e$. Note that $\vec{\alpha}_e = (\vec{d_a} - \vec{d_b})/\|\vec{d_a} - \vec{d_b}\|$, with $\vec{d}_.$ the 3D coordinates of the two detectors in coincidence.

Denote by $f(\vec{x})$ the tracer distribution and assume it is normalized, so that $f(\vec{x})$ is the probability distribution function (pdf) of having an emission at $\vec{x}$. The emission direction $\vec{\alpha}$ is isotropic. Assuming that scatter and randoms are negligible (or corrected), and that attenuation and sensitivity are taken into account by weighting each event, the pdf of detecting an event emitted at $\vec{x}$ along direction $\vec{\alpha} \in \Omega$ ($\Omega \in S^2$ defines the solid angle, and $|\Omega| = \int_\Omega d\vec{\alpha}$) with a most-likely annihilation point $\vec{x}_e$ is:

$$P(\vec{x}_e|\vec{x}, \vec{\alpha}) = \delta((\vec{x} - \vec{x}_e).\vec{\beta})\, \delta((\vec{x} - \vec{x}_e).\vec{\gamma})\, w((\vec{x} - \vec{x}_e).\vec{\alpha}) \tag{7}$$

with $\vec{\beta}$ and $\vec{\gamma}$ two unit vectors in the plane orthogonal to $\vec{\alpha}$. This conditional pdf is normalized because $\int dl\, w(l) = 1$. In the following, we calculate the expectation value of the first and second moments of inertia of the listmode TOF-PET emission data, assuming that the scanner has a uniform and shift invariant efficiency over the solid angle Ω.

7.2. First Moment

Define the vector of first order moments,

$$\hat{X} = \frac{1}{N} \sum_{e=1}^{N} \vec{x}_e. \tag{8}$$

Its expectation value is then, setting $\vec{x}_e = u\vec{\beta} + v\vec{\gamma} + l\vec{\alpha}$,

$$\begin{aligned} < \hat{X} > \; &= \int d\vec{x}\, f(\vec{x})\, \frac{1}{|\Omega|} \int_\Omega d\vec{\alpha} \int d\vec{x}_\epsilon\, P(\vec{x}_\epsilon|\vec{x}, \vec{\alpha})\, \vec{x}_\epsilon \\ &= \int d\vec{x}\, f(\vec{x})\, \frac{1}{|\Omega|} \int_\Omega d\vec{\alpha} \int du \int dv \int dl\, (u\vec{\beta} + v\vec{\gamma} + l\vec{\alpha}) \times \\ &\quad \delta((\vec{x}.\vec{\beta}) - u)\, \delta((\vec{x}.\vec{\gamma}) - v)\, w((\vec{x}.\vec{\alpha}) - l) \\ &= \int d\vec{x}\, f(\vec{x})\, \frac{1}{|\Omega|} \int_\Omega d\vec{\alpha}\, \vec{x} = \int d\vec{x}\, f(\vec{x})\, \vec{x}\, \frac{1}{|\Omega|} \int_\Omega d\vec{\alpha} = \vec{O} \end{aligned} \tag{9}$$

with

$$\vec{O} = \int d\vec{x}\, f(\vec{x})\, \vec{x}. \tag{10}$$

Equation (9) was obtained with the assumption that the solid angle Ω is independent of $\vec{x}$, and one thus obtains the expected result: equation (8) gives an unbiased estimation of $\vec{O}$, the center of mass of the tracer distribution.

7.3. Second Moment

Define the tensor of the second order moments,

$$\mathbf{T}_{i,j} = \frac{1}{N}\sum_{e=1}^{N}\{\|\vec{x}_e\|^2\delta_{i,j} - (\vec{x}_e)_i(\vec{x}_e)_j\} - \|\hat{X}\|^2\delta_{i,j} + \hat{X}_i\hat{X}_j \quad i,j = 1,2,3. \tag{11}$$

Calculating the following expectation value:

$$\begin{aligned}
< \frac{1}{N}\sum_{e=1}^{N}(\vec{x}_e)_i(\vec{x}_e)_j > \; &= \int d\vec{x}\, f(\vec{x})\, \frac{1}{|\Omega|}\int_\Omega d\vec{\alpha} \int d\vec{x}_\epsilon\, P(\vec{x}_\epsilon|\vec{x},\vec{\alpha})\, (\vec{x}_\epsilon)_i\, (\vec{x}_\epsilon)_j \\
&= \int d\vec{x}\, f(\vec{x})\, \frac{1}{|\Omega|}\int_\Omega d\vec{\alpha} \int du \int dv \int dl\, (u\vec{\beta} + v\vec{\gamma} + l\vec{\alpha})_i \times \\
&\quad (u\vec{\beta} + v\vec{\gamma} + l\vec{\alpha})_j\, \delta((\vec{x}.\vec{\beta}) - u)\, \delta((\vec{x}.\vec{\gamma}) - v)\, w((\vec{x}.\vec{\alpha}) - l) \\
&= \int d\vec{x}\, f(\vec{x})\, \frac{1}{|\Omega|}\int_\Omega d\vec{\alpha} \int dl'\, (\vec{x} + l'\vec{\alpha})_i\, (\vec{x} + l'\vec{\alpha})_j\, w(l') \\
&= \int d\vec{x}\, f(\vec{x})\, \vec{x}_i\, \vec{x}_j + \sigma^2 \frac{1}{|\Omega|}\int_\Omega d\vec{\alpha}\, \vec{\alpha}_i\, \vec{\alpha}_j
\end{aligned} \tag{12}$$

where we used $u\vec{\beta} + v\vec{\gamma} + l\vec{\alpha} = u\vec{\beta} + v\vec{\gamma} + (\vec{x}.\vec{\alpha})\vec{\alpha} - (\vec{x}.\vec{\alpha})\vec{\alpha} + l\vec{\alpha} = u\vec{\beta} + v\vec{\gamma} + (\vec{x}.\vec{\alpha})\vec{\alpha} + l'\vec{\alpha}$, $l' = l - (\vec{x}.\vec{\alpha})$, and $\int dl'\, l'\, w(l') = 0$. Inserting (12) in the definition of the tensor $\mathbf{T}$ defined from the list-mode data by (11), we obtain

$$(\frac{N}{N-1}) < \mathbf{T} >= \mathbf{I}^f + \mathbf{B} \tag{13}$$

with the inertia tensor of the object

$$\mathbf{I}^f_{i,j} = \int d\vec{x}\, f(\vec{x})\, \{\|\vec{x}\|^2\delta_{i,j} - \vec{x}_i\vec{x}_j\} - \|\vec{O}\|^2\delta_{i,j} + O_iO_j\delta_{i,j} \tag{14}$$

and the bias tensor

$$\mathbf{B}_{i,j} = \sigma^2 \frac{1}{|\Omega|}\int_\Omega d\vec{\alpha}\, \{\delta_{i,j} - \vec{\alpha}_i\vec{\alpha}_j\}. \tag{15}$$

Note that for any real scan $N >> 1$, hence the factor $N/(N-1)$ will be ignored below§.

The bias tensor (15) is proportional to the TOF resolution σ^2, and it is intuitively obvious that with perfect TOF resolution $< \mathbf{T} >= \mathbf{I}^f$. Applying a rotation to object f with some rotation matrix $\mathbf{R}$, the rotated object is $f_r(\vec{x}) = f(\mathbf{R}\vec{x})$, and its inertia tensor $\mathbf{I}^{f_r} = \mathbf{R}^T\mathbf{I}^f\mathbf{R}$. The bias tensor (15) however, depends on the scanner geometry, and thus remains unchanged. Therefore, the effect of the rotation on the estimator $\mathbf{T}$ is not simply given by the rotation:

$$< \mathbf{T}_r >= \mathbf{I}^{f_r} + \mathbf{B} \neq \mathbf{R}^T < \mathbf{T} > \mathbf{R} \tag{16}$$

§ This factor has the same origin as in the unbiased estimator of the variance of a data set.

If the TOF resolution is poor (also depending on the object), the bias (15) can be large leading to errors when $\mathbf{T}$ is used to estimate the rotation. Therefore correction for the bias prior to diagonalizing $\mathbf{T}$ and computing the rotation $\mathbf{R}$ becomes important. The results here were obtained assuming a shift invariant sensitivity, and in this simplified case the bias can be approximated. For the general case (the scanner aperture not being shift invariant) however, finding an approximation is not trivial.

7.4. Inertia Moments of Backprojections

The TOF backprojection of the listmode data is

$$\hat{b}(\vec{x}) = \frac{1}{N}\sum_{e=1}^{N} \delta((\vec{x}-\vec{x}_e).\vec{\beta}_e)\,\delta((\vec{x}-\vec{x}_e).\vec{\gamma}_e)\,w((\vec{x}-\vec{x}_e).\vec{\alpha}_e) \tag{17}$$

which is normalized such that $\int d\vec{x}\,\hat{b}(\vec{x}) = 1$. The center of mass of the backprojected data $\hat{b}$ is

$$\begin{aligned}
\hat{X} &= \int d\vec{x}\,\vec{x}\,\frac{1}{N}\sum_{e=1}^{N} \delta((\vec{x}-\vec{x}_e).\vec{\beta}_e)\,\delta((\vec{x}-\vec{x}_e).\vec{\gamma}_e)\,w((\vec{x}-\vec{x}_e).\vec{\alpha}_e) \\
&= \frac{1}{N}\sum_{e=1}^{N}\int du\int dv\int dl\,(\vec{x}_e + u\vec{\beta}_e + v\vec{\gamma}_e + l\vec{\alpha}_e)\,\delta(u)\,\delta(v)\,w(l) \\
&= \frac{1}{N}\sum_{e=1}^{N}\vec{x}_e
\end{aligned} \tag{18}$$

where we use as above the change of variable $\vec{x} = \vec{x}_e + u\vec{\beta}_e + v\vec{\gamma}_e + l\vec{\alpha}_e$ for event number e, and $\int dl\,l\,w(l) = 0$.

The inertia tensor of the backprojection is

$$\mathbf{I}^{\hat{b}}_{i,j} = \int d\vec{x}\,\hat{b}(\vec{x})\,\{\|\vec{x}\|^2\delta_{i,j} - \vec{x}_i\vec{x}_j\} - \|\hat{X}\|^2\delta_{i,j} + \hat{X}_i\hat{X}_j \tag{19}$$

Using (17) and the same change of variable as in (18),

$$\begin{aligned}
\int d\vec{x}\,\vec{x}_i\,\vec{x}_j\,\hat{b}(\vec{x}) &= \frac{1}{N}\sum_{e=1}^{N}\int du\int dv\int dl\,(\vec{x}_e + u\vec{\beta}_e + v\vec{\gamma}_e + l\vec{\alpha}_e)_i \times \\
&\qquad (\vec{x}_e + u\vec{\beta}_e + v\vec{\gamma}_e + l\vec{\alpha}_e)_j\,\delta(u)\,\delta(v)\,w(l) \\
&= \frac{1}{N}\sum_{e=1}^{N}\int dl\,(\vec{x}_e + l\vec{\alpha}_e)_i(\vec{x}_e + l\vec{\alpha}_e)_j\,w(l) \\
&= \frac{1}{N}\sum_{e=1}^{N}((\vec{x}_e)_i(\vec{x}_e)_j + \sigma^2(\vec{\alpha}_e)_i(\vec{\alpha}_e)_j)
\end{aligned} \tag{20}$$

where we use $\int dl\,l^2\,w(l) = \sigma^2$ and $\int dl\,l\,w(l) = 0$. One concludes that the inertia tensor of the backprojected listmode data can be calculated without explicitly building the backprojection image, as

$$\begin{aligned}
\mathbf{I}^{\hat{b}}_{i,j} = \frac{1}{N}\sum_{e=1}^{N}\Big(\|\vec{x}_e\|^2\delta_{i,j} - (\vec{x}_e)_i(\vec{x}_e)_j\Big) + \\
\sigma^2\frac{1}{N}\sum_{e=1}^{N}(\delta_{i,j} - (\vec{\alpha}_e)_i(\vec{\alpha}_e)_j) - \|\hat{X}\|^2\delta_{i,j} + \hat{X}_i\hat{X}_j
\end{aligned} \tag{21}$$

Comparing this result with (8), (11), and (12) we obtain

$$\mathbf{I}^{\hat{b}} = \mathbf{T} + \hat{\mathbf{B}} \tag{22}$$

Contrary to what intuition would suggest, the inertia tensor calculated from the backprojected image coincides with the inertia tensor of the most-likely annihilation points, up to a difference equal to $\hat{\mathbf{B}}$. Thus, although the backprojected image is less noisy than the image built as the set of most-likely annihilation points, this probably does not result in an improved variance when calculating the inertia tensor. Finally, using (13), and taking the expectation value of (22),

$$< \mathbf{I}^{\hat{b}} >=< \mathbf{T} > + < \hat{\mathbf{B}} >= \mathbf{I}^{f} + 2\mathbf{B} \tag{23}$$

The bias is therefore doubled by taking the backprojection, which seems logical since $w * w$ is a gaussian with variance $2\sigma^2$.

References

Buhler, P., U. Just, E. Will, J. Kotzerke, and J. v. d. Hoff (Sept. 2004). "An accurate method for correction of head movement in PET". *IEEE Transactions on Medical Imaging* 23.9, pp. 1176–1185.

Carson, R. E., W. C. Barker, Jeih-San Liow, and C. A. Johnson (Oct. 2003). "Design of a motion-compensation OSEM list-mode algorithm for resolution-recovery reconstruction for the HRRT". *2003 IEEE Nuclear Science Symposium. Conference Record (IEEE Cat. No.03CH37515)*. 2003 IEEE Nuclear Science Symposium. Conference Record (IEEE Cat. No.03CH37515). Vol. 5. ISSN: 1082-3654, 3281–3285 Vol.5.

de Jong, H. W. A. M., F. H. P. van Velden, R. W. Kloet, F. L. Buijs, R. Boellaard, and A. A. Lammertsma (Feb. 2007). "Performance evaluation of the ECAT HRRT: an LSO-LYSO double layer high resolution, high sensitivity scanner". *Physics in Medicine and Biology* 52.5, pp. 1505–1526.

Feng, T., D. Yang, W. Zhu, Y. Dong, and H. Li (Oct. 2016). "Real-time data-driven rigid motion detection and correction for brain scan with listmode PET". *2016 IEEE Nuclear Science Symposium, Medical Imaging Conference and Room-Temperature Semiconductor Detector Workshop (NSS/MIC/RTSD)*. 2016 IEEE Nuclear Science Symposium, Medical Imaging Conference and Room-Temperature Semiconductor Detector Workshop (NSS/MIC/RTSD), pp. 1–4.

Firouzian, A., A. Whittington, G. E. Searle, I. Koychev, G. Zamboni, S. Lovestone, R. N. Gunn, and on behalf of the Deep and Frequent Phenotyping study team (Mar. 2, 2018). "Imaging Aβ and tau in early stage Alzheimer's disease with [18F]AV45 and [18F]AV1451". *EJNMMI Research* 8.1, p. 19.

Fulton, R., I. Nickel, L. Tellmann, S. Meikle, U. Pietrzyk, and H. Herzog (Oct. 2003). "Event-by-event motion compensation in 3D PET". *2003 IEEE Nuclear Science Symposium. Conference Record (IEEE Cat. No.03CH37515)*. 2003 IEEE Nuclear Science Symposium. Conference Record (IEEE Cat. No.03CH37515). Vol. 5. ISSN: 1082-3654, 3286–3289 Vol.5.

Fulton, R. R., S. R. Meikle, S. Eberl, J. Pfeiffer, C. Constable, and M. J. Fulham (Oct. 2000). "Correction for head movements in positron emission tomography using an optical motion tracking system". *2000 IEEE Nuclear Science Symposium. Conference Record (Cat. No.00CH37149)*. 2000 IEEE Nuclear Science Symposium. Conference Record (Cat. No.00CH37149). Vol. 3. ISSN: 1082-3654, 17/58–17/62 vol.3.

Goldstein, S. R., M. E. Daube-Witherspoon, M. V. Green, and A. Eidsath (Feb. 1997). "A head motion measurement system suitable for emission computed tomography". *IEEE Transactions on Medical Imaging* 16.1, pp. 17–27.

Herzog, H., L. Tellmann, R. Fulton, I. Stangier, E. R. Kops, K. Bente, C. Boy, R. Hurlemann, and U. Pietrzyk (June 1, 2005). "Motion Artifact Reduction on Parametric PET Images of Neuroreceptor Binding". *Journal of Nuclear Medicine* 46.6, pp. 1059–1065.

Hill, D. L. G., P. G. Batchelor, M. Holden, and D. J. Hawkes (Feb. 2001). "Medical image registration". *Physics in Medicine and Biology* 46.3, R1–R45.

Hsu, D. F. C., E. Ilan, W. T. Peterson, J. Uribe, M. Lubberink, and C. S. Levin (Sept. 1, 2017). "Studies of a Next-Generation Silicon-Photomultiplier–Based Time-of-Flight PET/CT System". *Journal of Nuclear Medicine* 58.9, pp. 1511–1518.

Jin, X., C. Chan, T. Mulnix, V. Panin, M. E. Casey, C. Liu, and R. E. Carson (July 2013a). "List-mode reconstruction for the Biograph mCT with physics modeling and event-by-event motion correction". *Physics in Medicine and Biology* 58.16, pp. 5567–5591.

Jin, X., T. Mulnix, J.-D. Gallezot, and R. E. Carson (Oct. 2013b). "Evaluation of motion correction methods in human brain PET imaging—A simulation study based on human motion data". *Medical Physics* 40.10, p. 102503.

Kolinger, G. D., D. Vállez García, T. G. Lohith, E. D. Hostetler, C. Sur, A. Struyk, R. Boellaard, and M. Koole (May 27, 2021). "A dual-time-window protocol to reduce acquisition time of dynamic tau PET imaging using [18F]MK-6240". *EJNMMI Research* 11.1, p. 49.

Kyme, A. Z. and R. R. Fulton (June 8, 2021). "Motion estimation and correction in SPECT, PET and CT". *Physics in Medicine & Biology*.

Kyme, A. Z., S. Se, S. R. Meikle, and R. R. Fulton (May 2018). "Markerless motion estimation for motion-compensated clinical brain imaging". *Physics in Medicine & Biology* 63.10, p. 105018.

Lopresti, B. J., A. Russo, W. F. Jones, T. Fisher, D. G. Crouch, D. E. Altenburger, and D. W. Townsend (Dec. 1999). "Implementation and performance of an optical

motion tracking system for high resolution brain PET imaging". *IEEE Transactions on Nuclear Science* 46.6, pp. 2059–2067.

Lu, Y., M. Naganawa, T. Toyonaga, J.-D. Gallezot, K. Fontaine, S. Ren, E. M. Revilla, T. Mulnix, and R. E. Carson (Sept. 2020). "Data-Driven Motion Detection and Event-by-Event Correction for Brain PET: Comparison with Vicra". *Journal of Nuclear Medicine* 61.9, pp. 1397–1403.

Menke, M., M. S. Atkins, and K. R. Buckley (Feb. 1996). "Compensation methods for head motion detected during PET imaging". *IEEE Transactions on Nuclear Science* 43.1, pp. 310–317.

Noonan, P. J., J. Howard, W. A. Hallett, and R. N. Gunn (Nov. 2015). "Repurposing the Microsoft Kinect for Windows v2 for external head motion tracking for brain PET". *Physics in Medicine and Biology* 60.22, pp. 8753–8766.

Olesen, O. V., J. M. Sullivan, T. Mulnix, R. R. Paulsen, L. Hojgaard, B. Roed, R. E. Carson, E. D. Morris, and R. Larsen (Feb. 2013). "List-Mode PET Motion Correction Using Markerless Head Tracking: Proof-of-Concept With Scans of Human Subject". *IEEE Transactions on Medical Imaging* 32.2, pp. 200–209.

Panin, V. (Jan. 20, 2021). "Histo-Projections TOF Data Non-Rigid Motion Estimation and Correction".

Rahmim, A., P. Bloomfield, S. Houle, M. Lenox, C. Michel, K. Buckley, T. Ruth, and V. Sossi (Oct. 2004). "Motion compensation in histogram-mode and list-mode EM reconstructions: beyond the event-driven approach". *IEEE Trans. Nucl. Sci.* 51.5, pp. 2588–2596.

Reilhac, A., G. Batan, C. Michel, C. Grova, J. Tohka, D. L. Collins, N. Costes, and A. C. Evans (Oct. 2005). "PET-SORTEO: validation and development of database of Simulated PET volumes". *IEEE Transactions on Nuclear Science* 52.5, pp. 1321–1328.

Ren, S., X. Jin, C. Chan, Y. Jian, T. Mulnix, C. Liu, and R. E. Carson (May 2017). "Data-driven event-by-event respiratory motion correction using TOF PET list-mode centroid of distribution". *Physics in Medicine and Biology* 62.12, pp. 4741–4755.

Ruttimann, U. E., P. J. Andreason, and D. Rio (May 31, 1995). "Head motion during positron emission tomography: is it significant?" *Psychiatry Research: Neuroimaging* 61.1, pp. 43–51.

Schönemann, P. H. (Mar. 1, 1966). "A generalized solution of the orthogonal procrustes problem". *Psychometrika* 31.1, pp. 1–10.

Spangler-Bickell, M. G., T. W. Deller, V. Bettinardi, and F. Jansen (Feb. 1, 2021). "Ultra-Fast List-Mode Reconstruction of Short PET Frames and Example Applications". *Journal of Nuclear Medicine* 62.2, pp. 287–292.

Spangler-Bickell, M. G., M. M. Khalighi, C. Hoo, P. S. DiGiacomo, J. Maclaren, M. Aksoy, D. Rettmann, R. Bammer, G. Zaharchuk, M. Zeineh, and F. Jansen (July 2019). "Rigid Motion Correction for Brain PET/MR Imaging Using Optical

Tracking". *IEEE Transactions on Radiation and Plasma Medical Sciences* 3.4, pp. 498–503.

van Sluis, J. J., J. de Jong, J. Schaar, W. Noordzij, P. van Snick, R. Dierckx, R. Borra, A. Willemsen, and R. Boellaard (Jan. 1, 2019). "Performance characteristics of the digital Biograph Vision PET/CT system". *Journal of Nuclear Medicine*.